ACS Catalysis
Research Article
pubs.acs.org/acscatalysis

Borohydride Electrooxidation on Carbon-Supported Noble Metal Nanoparticles: Insights into Hydrogen and Hydroxyborane Formation

Anielli M. Pasqualeti,[†] Pierre-Yves Olu,[‡,§] Marian Chatenet,[‡,§,∥] and Fabio H. B. Lima*,[†]

[†]Institute of Chemistry of Sao Carlos - University of Sao Paulo, CEP 13560-970, CP 780 Sao Carlos, Sao Paulo, Brazil
[‡]Université Grenoble Alpes, LEPMI, F-38000 Grenoble, France
[§]CNRS, LEPMI, F-38000 Grenoble, France
[∥]French University Institute, 75005 Paris, France

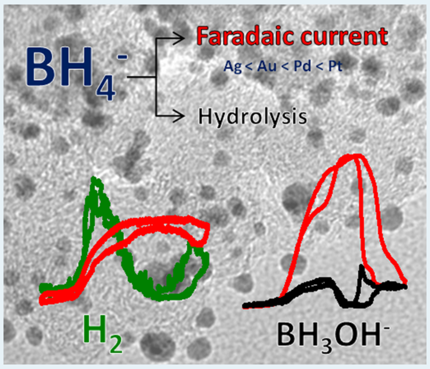

ABSTRACT: Borohydride anions (BH_4^-) are interesting as fuel for low-temperature alkaline fuel cells, owing to their high hydrogen content and low theoretical potential of oxidation. However, the borohydride electrooxidation mechanism and the potential dependence of the undesirable parallel hydrolysis pathway are not completely understood. In this study, by using a dual thin-layer flow-cell online coupled with a mass spectrometer and a rotating ring-disk electrode, the electrocatalytic activity and the dependence of the molecular hydrogen and hydroxiborane (BH_3OH^-) formation were investigated for carbon-supported Au, Ag, Pt, and Pd nanoparticles. For Au/C and Ag/C, the H_2 and BH_3OH^- production presented a peak in the potential region of the first branch of the BOR wave and another increase in the metal oxide region. Pt/C and Pd/C showed accentuated H_2 detection at the OCP, with a sharp decrease to practically zero after the BOR onset. Interestingly, and contrarily to what was observed for Au/C and Ag/C, the RRDE measurements showed BH_3OH^- production only at higher potentials (Pt- or Pd-oxides). These results were explained on the basis of the higher reactivity of Pt/C and Pd/C for the BOR, in which BH_x-like species remain adsorbed and hydrogen is consumed via electrooxidation on their surfaces, at low potentials. On the other hand, Au/C and Ag/C, possessing lower reactivity (lower *d*-band center), the BH_3-like species, produced in the first BOR steps, desorb from their surfaces and are detected at the ring. Concomitantly, at the BOR onset, H_2 is formed, via recombination of adsorbed hydrogen atoms and can be detected by the mass spectrometer because these materials are relatively inactive for the hydrogen oxidation reaction.

KEYWORDS: *borohydride electrooxidation reaction (BOR), borohydride heterogeneous hydrolysis, alkaline fuel cells, carbon-supported nanoparticles, online DEMS*

1. INTRODUCTION

Technologies that enable the production of sustainable and renewable energy, as well as use in efficient conversion devices, offer great potential to meet a future environmentally friendly scenario. This is particularly stringent for off-the-grid power, in which internal-combustion engines are currently among the most-widely employed systems, definitely consisting in a nonsustainable solution. For two decades, lithium-ion batteries have been extensively used for powering different types of devices, owing to their high energy density and reasonable cost. Great efforts have since been made to raise their energy densities, as a result of the challenging demands of electric or hybrid vehicles. However, the low storage capacity, intrinsic to closed electrochemical generators, limits their autonomy.[1] In this scenario, fuel cells, operating at low temperature, are a promising technology for increasing the overall system autonomy, because they can be an on-board energy source for recharging lithium-ion batteries.

Alkaline fuel cells that operate with borohydride exhibit a high theoretical voltage (1.64 V) due to the low reversible thermodynamic potential ($E^0 = -1.24$ V vs NHE − eq 1) of the electrooxidation of borohydride anion (BH_4^-).[2−10] The so-called direct borohydride fuel cell (DBFC) consists of the combination of an anode, in which the borohydride electrooxidation reaction (BOR) takes place (eq 1) and a cathode, where the oxygen electroreduction reaction (ORR) occurs (eq 2).[11−23]

Anode:

$$BH_4^- + 8OH^- \rightarrow BO_2^- + 6H_2O + 8e^- \quad (E^0 = -1.24 \text{ V vs NHE}) \; (\text{pH} = 14) \qquad (1)$$

Cathode:

Received: January 19, 2015
Revised: March 17, 2015
Published: March 19, 2015

DOI: 10.1021/acscatal.5b00107
ACS Catal. 2015, 5, 2778−2787

$$O_2 + 2H_2O + 4e^- \rightarrow 4OH^- \quad (E^0 = 0.40 \text{ V vs NHE}) \ (\text{pH} = 14) \tag{2}$$

Global reaction:

$$BH_4^- + 2O_2 \rightarrow BO_2^- + 2H_2O \quad (\Delta E = 1.64 \text{ V}) \tag{3}$$

The complete electrooxidation of sodium borohydride presents several difficulties associated both to the reaction kinetics and mechanism, due to the transfer of eight electrons.[24−31] The BOR mechanism involves B−H bond breaking steps, followed by oxygen addition for the electrooxidation of the adsorbed hydrogen atoms. The elementary reactions can be described by the following sequence (eqs 4−6), proposed for Pt surfaces or surfaces prone to fast dehydridation of the BH_4^- species, even at potential values as low as 0.05 V vs RHE:[32−35]

$$BH_4^-{}_{(aq)} + 4* \rightarrow BH* + 3H* + e^- \tag{4}$$

$$BH* + OH^-{}_{(aq)} + * \rightarrow BOH* + H* + e^- \tag{5}$$

$$BOH* + 2OH^-{}_{(aq)} \rightarrow B(OH)_3* + 2e^- \tag{6}$$

(where * refers to an active surface site of the metal electrocatalyst)

Considering these reaction steps, the B−H bond activation may result in subsequent electrooxidation or in hydrolysis, depending on the resulting metal surface coverage of hydrogen (H*, also noted H_{ad}), which all depend on the reactivity of the metal electrocatalyst and electrode potential. If the surface H_{ad} coverage resulting from B−H bond activation exceeds the saturation H_{ad} coverage, hydrogen gas evolution will occur through eq 7, which is only likely for low potentials values (or for surfaces not active for H* ionization, like Au and Ag, see below):

$$H* + H* \rightarrow H_2 \tag{7}$$

Conversely, the electrooxidation of the H* species (eq 8) becomes favorable at higher overpotentials ($E > 0$ V vs RHE):

$$H* + OH^- \rightarrow H_2O + e^- \tag{8}$$

Overall, the competition between the "direct" electrooxidation of BH_4^- (sequence of eqs 4−6, 8) and the "indirect" electrooxidation of BH_4^-, that is, the heterogeneous hydrolysis followed by valorization of the formed H_2 (eqs 9 and 10), will determine the faradaic efficiency of the BH_4^- conversion, as summarized in eq 11.

$$BH_4^- + 2H_2O \rightarrow BO_2^- + 4H_2 \tag{9}$$

$$H_2 + 2OH^- \rightarrow 2H_2O + 2e^- \tag{10}$$

$$BH_4^- + xOH^- = BO_2^- + (x - 2)H_2O + (4 - 0.5x)H_2 + xe^- \tag{11}$$

where x is an integer between 0 and 8.

Devices that operate with anode electrocatalysts that preferentially catalyze the reaction via the hydrolysis pathway (H_2 formation), and that are at the same time active for H_2 electrooxidation, may yield near-complete faradic efficiency: eight electrons can be produced if all hydrogen molecules react on the electrocatalyst surface (which is unlikely due to natural diffusion issues). It is worth noting, however, that this reaction route wastes some of the chemical energy stored in the fuel, due to the exothermic hydrolysis reaction, representing an energy drop of approximately 25% when compared to the direct electrooxidation of BH_4^- into BO_2^- (H_2 is valorized at 0 V vs RHE, versus −0.4 V vs RHE for BH_4^-, in theory).[34] Therefore, the detection of H_2 and other reaction byproducts (such as BH_3OH^-) becomes important for monitoring the hydrolysis pathway and, consequently, for the determination of the reaction efficiency for an particular electrocatalyst.[1,2] This aspect will be further discussed in the next sections.

The direct electrooxidation of BH_4^- to BO_2^- should result in the maximum faradaic efficiency and, therefore, increases the energy output, which is the desired reaction pathway for direct borohydride fuel cells. However, several DBFC anode materials yield a poor overall faradaic efficiency, due to considerable H_2 production and subsequent losses. Consequent efforts aimed at developing materials in order to increase the fuel utilization or the number of exchanged electrons per BH_4^- species.[36−40] Nevertheless, even for the most studied metal electrocatalysts for DBFC anodes, such as Au/C, Ag/C and Pt/C,[41−43] up to now, there is lack of consensus and not enough knowledge about the dependence of the hydrolysis pathway and of the faradaic efficiency of the BOR versus electrode potential. The investigation of the hydrolysis pathway during the borohydride electrooxidation reaction can be achieved by monitoring H_2 by online techniques, such as differential electrochemical mass spectrometry (DEMS), as recently attempted for Au or Pt surfaces.[44,45] However, the investigation using stagnant electrolyte cell (the usual setup in DEMS) is limited for carbon-supported electrocatalysts, due to the required use of an electron-conducting substrate to support the working electrode (i.e., where the carbon-supported electrocatalyst is deposited), which is located in the interface with the high vacuum chamber of the mass spectrometer.[46] This substrate, necessarily porous, normally consists of a sputtered Au layer, which may affect the response of the investigated carbon-supported electrocatalyst, because Au is active for the BOR and its hydrolysis.[44,45] This limitation can be overcome by using the dual thin-layer flow cell.[46] In this setup, the electrolyte flows through capillaries, gets in contact with the working electrode in a wall-jet configuration, and it is then directed to a detection chamber which is in contact with the interface with the high vacuum of the mass spectrometer. This configuration enables using different kinds of working electrodes and substrates. Particularly, glassy carbon, which is not active for the BOR, can be used as a substrate for depositing powder carbon-supported electrocatalysts, enabling the investigation of the mass signals originating only from the material under study and not from the substrate.

Considering the above-mentioned aspects, the objectives of the present work were related to the investigation of the electrocatalytic activity of carbon-supported Au, Ag, Pt, and Pd nanoparticles. The hydrolysis pathway was monitored following the molecular hydrogen formation by online DEMS measurements. The obtained faradaic current and the DEMS ionic signal were combined in order to estimate the potential-dependent number of electrons involved in the BOR for the different investigated materials. Besides, the possible formation of hydroxyborane was surveyed using the gold-ring rotating ring-disk electrode (RDDE) technique, as initially performed by Krishnan et al.[47]

2. EXPERIMENTAL SECTION

The electrocatalysts were formed by Au, Ag, Pt, and Pd metallic nanoparticles (20 wt %) supported on carbon-black powder (Vulcan XC-72R, composed of primary carbon nanoparticles of 20−30 nm diameter). The corresponding Au/C, Ag/C, Pt/C, and Pd/C materials were synthesized via chemical reduction with $NaBH_4$, in the presence of sodium citrate. In this method, an appropriate amount of the noble metal precursor salts ($HAuCl_4$, $AgNO_3$, H_2PtCl_4 or $PdCl_2$, all from Sigma-Aldrich), was dissolved in 1.6 L of ultrapure water (18.2 MΩ cm, Millipore), containing 0.2 g of sodium citrate[48−50] (in the case of $PdCl_2$, HCl was added to facilitate the salt dissolution). The flask was transferred to a magnetic stirring plate, and this was followed by a rapid addition of 50 mL of an aqueous solution containing 0.06 g of sodium borohydride and 0.2 g of sodium citrate. A suspension containing an appropriate quantity of Vulcan XC-72R carbon-black powder (to result in 80 wt %) in water, previously kept in an ultrasound bath during 20 min, was added to the resulting colloidal nanoparticle suspension and kept under magnetic stirring during 48 h for the total anchoring of the metal nanoparticles onto the carbon-black powder. This step was followed by filtration and rinsing several times with ultrapure water. The resulting carbon-supported electrocatalysts were kiln-dried at 70 °C for 24 h.

The atomic compositions of the resulting catalysts were estimated by X-ray energy dispersive spectroscopy (X-EDS) analysis, using a Zeiss-Leica/LEO 440 model (LEO, U.K.) scanning electron microscopy (SEM) with a Link Analytical microanalyzer (Isis System Series 200). Physical properties such as crystallographic structure and average crystallite size were estimated by X-ray diffraction measurements (XRD, Rigaku Ultima IV), carried out in the scan axis 2θ range from 25° up to 100°, and using Cu $K\alpha$ radiation (1.542 Å) with a scan rate of 0.5° min^{-1}. The average crystallite sizes were estimated from the (111) peak of the metal diffraction patterns (all of face-centered cubic structure), using the Scherrer equation.[51] The distribution of the metal nanoparticles on the carbon powder support and the particle sizes were investigated by Transmission Electron Microscopy (TEM) imaging, using a Jeol 2010 microscope, with a LaB_6 filament and operated at 200 kV accelerating voltage (point-to-point resolution of 0.19 Å). The samples for the TEM measurements were prepared by ultrasonically treating the catalyst powders in isopropyl alcohol. A drop of the resulting dispersion was placed on thin carbon films deposited on standard TEM copper grids and dried in air. The images were acquired by observing ca. 20 different areas of the samples, in order to enable statistically relevant observations. The diameters of the catalyst particles were measured from the TEM images using the ImageJ software. At least 300 isolated (i.e., not agglomerated) nanoparticles of each sample were counted to build the size distribution histograms (see ref 52 for details).

The electrochemical measurements were performed using 1.0 mol L^{-1} NaOH as supporting electrolyte, with the presence or the absence of $NaBH_4$ at 1.0 or 10.0 mmol L^{-1}, depending on the experiment. All electrolytic solutions were prepared from high purity salts (Merck Suprapur or Sigma-Aldrich) and ultrapure water. A conventional electrochemical cell, equipped with a water jacket, was used for Rotating Ring Disk Electrode (Pine Instruments) (RRDE) measurements (collection efficiency of 23%). In this system, an interchangeable glassy carbon disk (5 mm diameter, 0.196 cm^2 - with a Teflon shroud insulating the disk) was used as working electrode, in which the metal nanoparticle electrocatalysts were deposited. A gold ring electrode was employed as a sensor to detect the BH_3OH^- species produced in the working disk electrode. This was made measuring the magnitude of the BH_3OH^- oxidation current at a constant potential of ≈ −0.72 V vs Hg/HgO/OH^- (0.2 V vs RHE), where the BH_4^- oxidation current is negligible for the investigated electrocatalysts. In all measurements, the temperature was maintained constant at 25.0 ± 0.1 °C, using a Cole-Parmer Polystat temperature controller. An Au foil and a Hg/HgO/OH^- in the same electrolyte were used as counter and reference electrodes, respectively (all potentials are referred here to that of Hg/HgO/OH^-, NaOH 1.0 mol L^{-1}). The cyclic voltammetries were recorded at 5.0 mV s^{-1} or 20 mV s^{-1}, depending on the experiment, and the electrolyte was saturated with purified N_2. All the experiments were conducted using an Autolab potentiostat (PGSTAT 30).

For the RRDE measurements, a suspension of 2.0 mg mL^{-1} of M/C (M = Au, Ag, Pt or Pd) was prepared, dispersing the catalyst powder in isopropyl alcohol using an ultrasound bath. A 20 μL aliquot of the dispersed suspension was pipetted and deposited onto the top of the RRDE disc electrode and dried under vacuum. After the evaporation of the isopropyl alcohol of the suspension, 10 μL of a diluted Nafion solution (prepared from a 5% solution, Aldrich) was deposited onto the surface of the M/C thin layer in order to attach the catalytic particles on the disk electrode substrate.

Online DEMS measurements were performed with a Pfeiffer Vacuum QMA 200 quadrupole mass spectrometer using a setup consisting of two differentially pumping chambers.[53,54] The method allows the online detection of volatile and gaseous products of electrochemical reactions during the application of a potential scan. In a typical DEMS experiment, the current vs potential curves are recorded simultaneously with the mass intensity vs potential curves, for selected values of m/z (mass/charge) ionic signals. The working electrodes for the DEMS experiments were prepared in a similar manner than that for RRDE, pipetting 20 μL of an aqueous suspension of the electrocatalyst and depositing onto a glassy carbon rod (9.0 mm diameter—the area to deposit the electrocatalyst was limited to 0.196 cm^2 in order to keep the same area used in the RRDE measurements), followed by dropping 10 μL of a diluted Nafion solution onto the glassy carbon rod. The electrodes were placed into a dual thin-layer flow cell, which was constructed following the schematics of previous published works.[53,55] The working electrode was pressed against a ca. 0.025 cm thick Teflon spacer. This produced an exposed area of ca. 0.31 cm^{-2} and an electrolyte volume of ca. 0.0077 cm^3, which is the reaction chamber. The chamber located below the detection compartment resulted in a volume of 0.013 cm^3, and it was separated from the high vacuum chamber of the mass spectrometer using a porous PTFE membrane (Gore-Tex pore size 0.02 and 50 μm thick). The electrolyte flow rate was set at ca. 15 μL s^{-1}, and it was obtained by using a syringe pump. In the DEMS measurements, the concentration of BH_4^- was 1.0 mmol L^{-1} in order to avoid extensive H_2 bubbles formation, originating from its homo/heterogeneous hydrolysis in the capillary tube of the flow cell.[56,57] Two platinum wires at the inlet and outlet of the thin-layer cell, connected through an external resistance (typically 3 MΩ), were used as counter electrodes. Hg/HgO/OH^-, connected to the outlet of the DEMS cell via a Teflon capillary, served as a reference electrode. For all DEMS measurements, the scan rate was 5.0

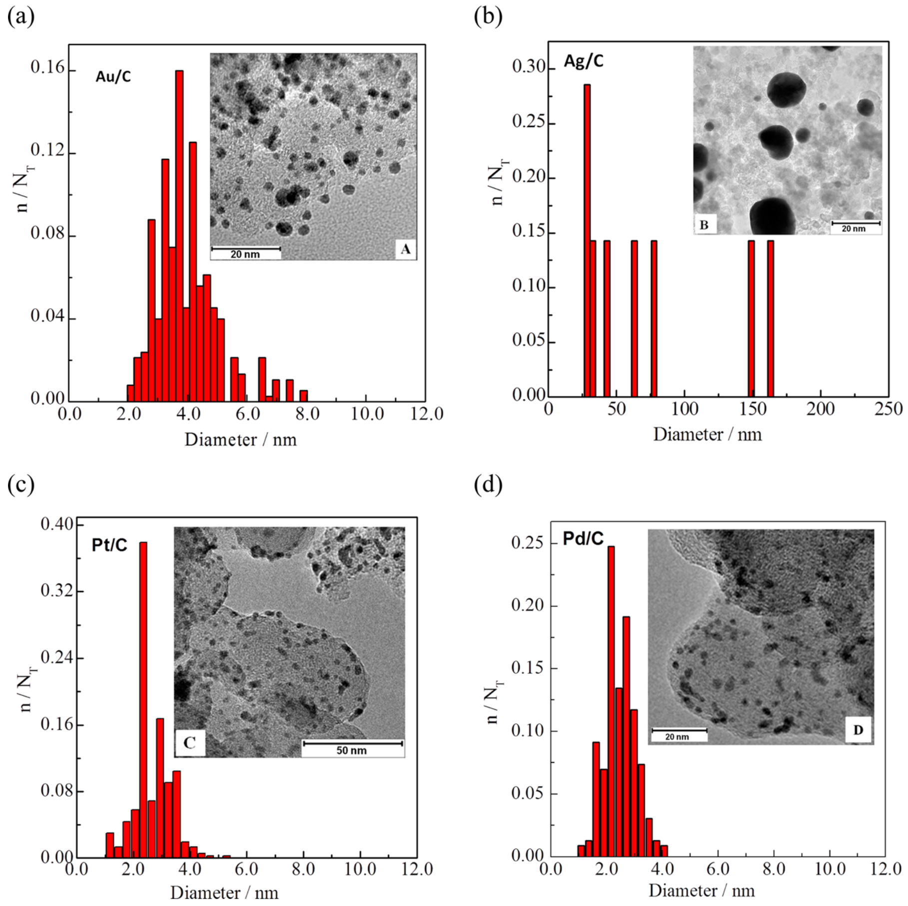

Figure 1. Transmission electron microscopy images and their corresponding particle size distribution histograms for the different carbon-supported nanoparticles: (a) Au/C, (b) Ag/C, (c) Pt/C, and (d) Pd/C.

Table 1. Structural Features Obtained by X-ray Diffraction and HRTEM Measurements

electrocatalyst	EDX − metal wt % on carbon	XRD − calculated lattice parameter/nm	lattice parameter − (literature)/nm	XRD − calculated average crystallite size/nm	TEM − average particle size/nm
Au/C	21%	0.4077	0.4078	6.3	3.7
Ag/C	19%	0.4090	0.4085	27.1	25−175
Pt/C	20%	0.3923	0.3924	6.2	2.5
Pd/C	19%	0.3894	0.3890	2.8	2.4

mV s^{-1}, and the formation of molecular hydrogen was monitored at $m/z = 2$, as a function of the electrode potential.

3. RESULTS AND DISCUSSION

3.1. Characterization of the Nanoparticles. The metal particle distribution on the carbon-black support and particle size were both investigated by TEM. Figure 1a−d show the representative bright-field images and the particle size distribution histograms for Au/C, Ag/C, Pt/C, and Pd/C, respectively. The images reveal homogeneous distribution of the metal nanoparticles on the carbon-black support, except for Ag/C. The average particle sizes were estimated from (isolated) particle distribution histograms, and the obtained values are summarized in Table 1 (together with other physical parameters). As can be observed, the histogram for Au/C shows a broad particle size distribution, with most of the particles presenting diameters in the range of 3−8 nm, with an average of ca. 3.7 nm. Ag/C shows the presence of large particles, with diameters in the range of 25−175 nm. Pt/C and Pd/C presented the smallest particle sizes, with average diameters of 2.5 and 2.4 nm, respectively.

The results of the X-EDS measurements, obtained using conventional SEM equipment, demonstrated that the metal to carbon ratios were close to the forecast of 20 wt % for all investigated materials (the authors acknowledge that this technique bares a non-negligible intrinsic uncertainty). The crystallite structures of the as-prepared Au/C, Ag/C, Pt/C, and Pd/C nanoparticles were determined using X-ray diffraction (XRD) measurements, and the obtained diffraction patterns are presented in Figures 2. The five main characteristic peaks of the face-centered cubic (fcc) structure, namely, the (111), (200), (220), (311), and (222) planes, can be observed for all investigated materials. The values of the lattice parameters and the average crystallite sizes were calculated using the Scherrer equation and are presented in Table 1. The lattice parameters are lower for Pd and Pt when compared to those for Ag and Au, which is consistent with the smaller atomic radii of the Pd and Pt atoms. The obtained values of the lattice parameters are very close to those of the corresponding bulk metals (also included

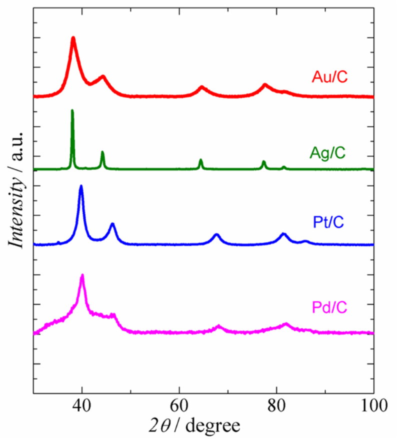

Figure 2. X-ray powder diffraction intensities for the synthesized nanoparticles as indicated in the figure insets.

in Table 1), which rules out any electronic structural change of the investigated materials due to the nanometric dimensions. The crystallite sizes are in agreement with the trend observed by TEM for Pd/C. For both Pt/C and Au/C, the TEM sizes are not in agreement with the crystallite sizes obtained from the XRD data, and this may arise from the existence of some large particles or agglomerates which were not taken into account in TEM histograms. For Ag/C, the results show very large crystallites and particle sizes (TEM). Therefore, this material presents much lower surface area when compared to the other investigated materials.

3.2. Electrochemical Experiments. *3.2.1. Online Differential Electrochemical Mass Spectrometry.* Typical voltammograms of the M/C catalysts in alkaline supporting electrolyte (in absence of BH_4^-), obtained using the wall-jet configuration of the dual thin-layer flow cell are displayed as insets of Figure 3a–d. Those for Au/C and Ag/C only exhibit regions of formation and reduction of oxygenated species, as such catalysts are relatively inactive for hydrogen adsorption/desorption. In contrast, the voltammograms for Pt/C and Pd/C feature clear hydrogen adsorption/desorption peaks, highlighting the ability of these metal for the breaking of water molecule bonds.

As mentioned before, a flow cell was operated for H_2 detection during the BOR on the synthesized M/C electrocatalysts. Aiming at a quantitative determination of the amount

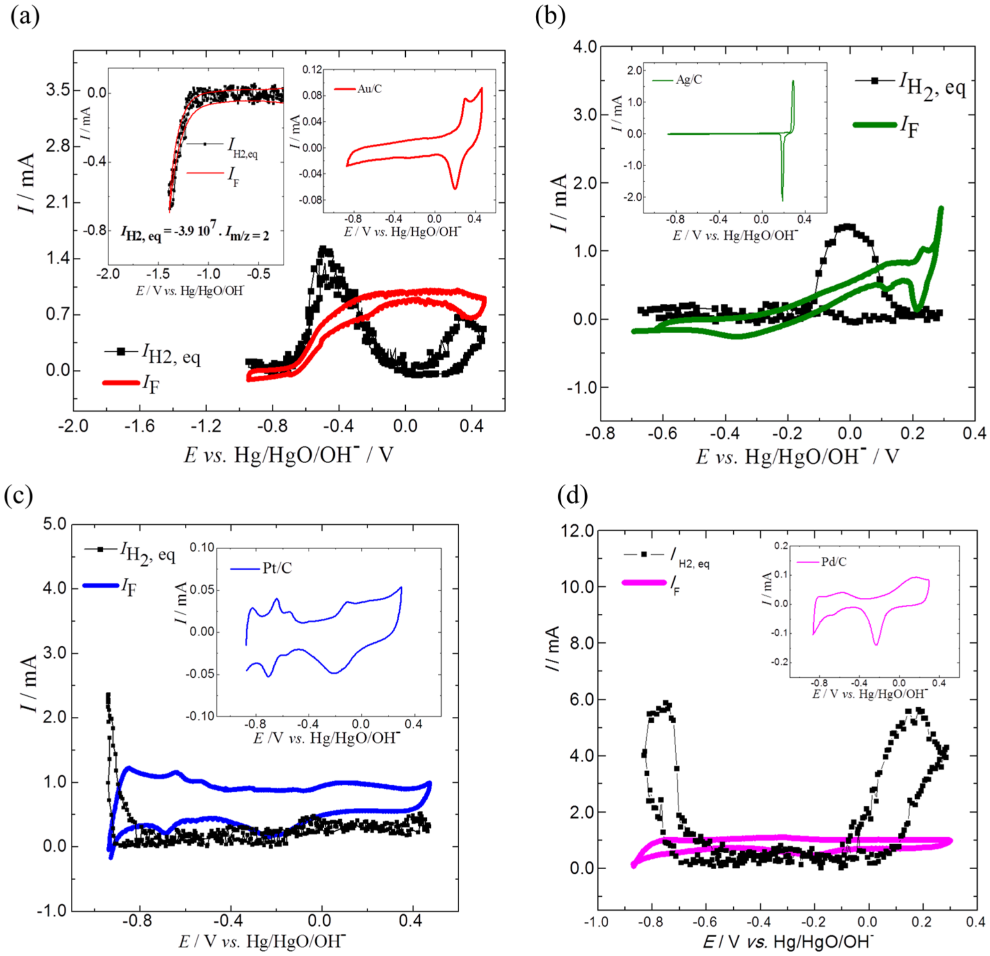

Figure 3. Faradaic current for the BOR and ionic current for $m/z = 2$ (H_2) detection converted into an equivalent HER current ($I_{H2,eq}$) obtained during DEMS experiments of cyclic voltamemtry for the different investigated electrocatalysts in 1.0 mmol L^{-1} BH_4^- + 1.0 mol L^{-1} NaOH electrolyte at 25 °C, in Ar-saturated solution; each CV was obtained at a scan rate of 5.0 mV s^{-1}, and the electrolyte flow rate was at ca. 15 μL s^{-1}. (a) Au/C (inset, left: example of the HER faradaic current and of the ionic signal for molecular hydrogen detection obtained during the calibration procedure for the Au/C electrode), (b) Ag/C, (c) Pt/C, and (d) Pd/C (the insets show the CV obtained for the investigated metal nanoparticles in Ar-saturated 1.0 mol L^{-1} NaOH electrolyte at 5.0 mV s^{-1}).

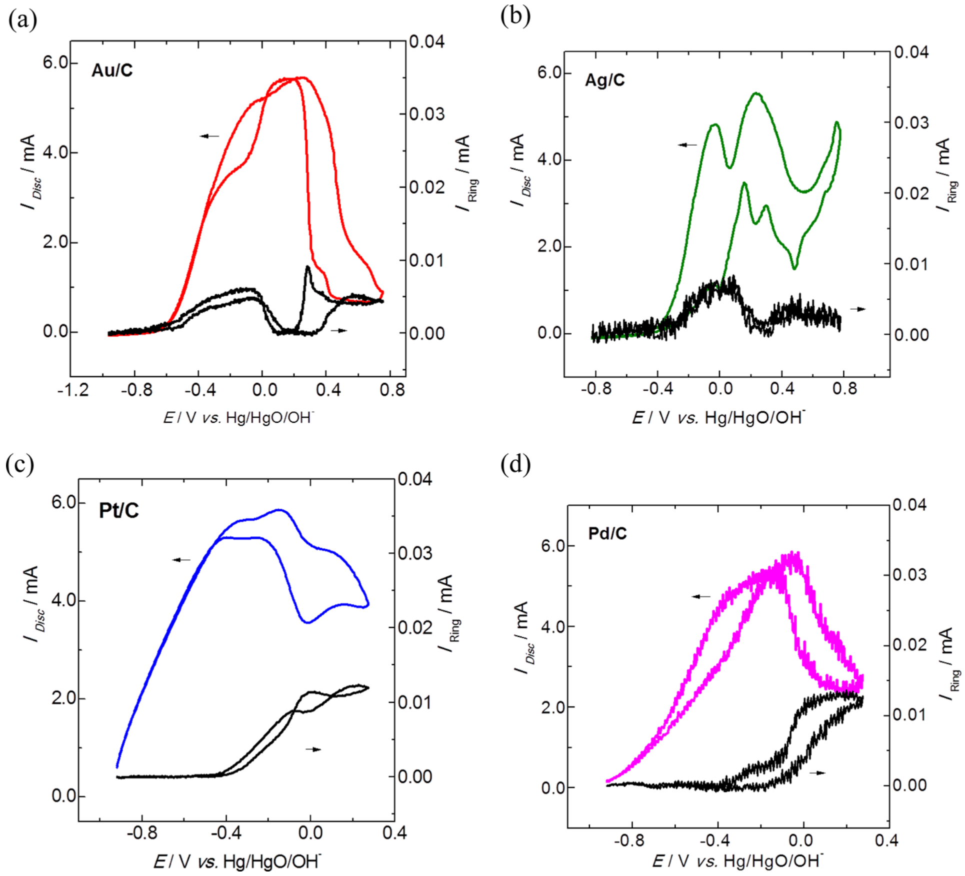

Figure 4. Rotating-ring disk electrode measurements with the faradaic current for the BOR (disk) and the faradaic current for the hydroxiborane detection (ring) for the different investigated electrocatalysts in 1.0 mmol L^{-1} BH_4^- + 1.0 mol L^{-1} NaOH electrolyte at 25 °C, in Ar-saturated solution; each CV was obtained at a scan rate of 5.0 mV s^{-1} and with a rotating rate of 1660 rpm; (a) Au/C, (b) Ag/C, (c) Pt/C, and (d) Pd/C.

of hydrogen evolved, the DEMS setup was first calibrated with respect to the evolution of molecular hydrogen for the different electrodes investigated. For that purpose, H_2 was deliberately evolved (HER − inverse of eq 10) imposing a slow negative-going potential scan in the supporting electrolyte, while the H_2 signal (m/z = 2) was concomitantly monitored. The plot of ionic current for H_2 detection versus faradaic current for H_2 evolution (HER) was utilized for the calculation of the DEMS constant (K) for each investigated electrode. These constants were used to convert the mass current ($I_{m/z=2}$) into an equivalent HER current ($I_{\mathrm{H2,\ eq}}$), using eq 12, according to the procedure described in ref 45. The calibration curve obtained for the Au/C electrode is presented in Figure 3a (inset, left), as an example. It shows the faradaic current for the hydrogen evolution reaction and the ionic current for the detection hydrogen (this procedure was conducted for all investigated electrodes, but it is not shown here for brevity).

$$I_{\mathrm{H2,eq}} = K{*}I_{\mathrm{m/z=2}} \qquad (12)$$

Figure 3a−d also present the faradic current for the BOR and the corresponding $I_{\mathrm{eq,H2}}$ obtained during DEMS experiments. The overall analysis of the BOR faradic current in the DEMS flow cell shows the following trend in activity: Pt/C > Pd/C > Au/C > Ag/C. The comparison of the ionic current for the H_2 detection reveals similar behavior for Au/C and Ag/C on the one side and for Pt/C and Pd/C on the other side. In the former case, $I_{\mathrm{H2,eq}}$ increases with the BOR faradaic current (starting at the reaction onset), indicating a competition between the direct borohydride oxidation reaction and the evolution of hydrogen (a sign of heterogeneous hydrolysis).[58−60] The H_2 evolution defines an ionic current peak at ca. −0.5 V for Au/C and at ca. 0.0 V for Ag/C, after which the H_2 production decreases; for Au/C, it increases again in the potential domain of Au-oxide(hydroxide) formation. The positive and the negative-going scans for Au/C have similar profiles for the faradaic and H_2 ionic current. Conversely, the negative-going scan for Ag/C shows much smaller ionic current when compared to the positive-going scan. The reason for such behavior is not completely understood because the BOR faradaic current at Ag/C still remains in the negative-going scan, but knowing this happens at potentials that are irrelevant to the DBFC anode, it will not be discussed further.

The online DEMS measurements obtained for Pt/C and Pd/C, presented in Figures 3c,d, show similar BOR onset potential, ca. −0.9 V; in addition, the BOR faradaic current extends to the whole investigated potential domain. Interestingly, the profile of the faradaic currents for Pt/C and Pd/C obtained during the potentiodynamic measurements in the presence of BH_4^- exhibit an envelope close to that measured in supporting NaOH electrolyte but shifted to positive currents. This resulting profile is ascribed to the sum of the faradaic current of the BOR and the pseudocapacitive currents related to the hydrogen adsorption/desorption, oxide formation/reduction processes that take place on the platinum and palladium surfaces. With larger BH_4^- concentrations, the BOR currents largely exceed the pseudocapacitive currents recorded in the absence of BH_4^-, but the DEMS measurement is impracticable due to the extensive H_2 bubbles formation and pressure buildup (from homo/heterogeneous hydrolysis) in the capillaries of the flow cell. Additionally, it can be noted that the heterogeneous hydrolysis is very intense at the OCP for Pt/C and Pd/C. As can be observed, these metals yield some H_2 production at OCP, followed by a drastic reduction as soon as the BOR starts and an increase at the Pt or Pd-hydroxide/oxide region.

3.2.2. Rotating Ring-Disk Electrodes. The electrocatalytic activities of the different M/C materials were also investigated using RRDE. Figure 4a−d shows the comparison of the positive and negative-going scans during potentiodynamic curves, obtained at 1600 rpm, for the electrooxidation of 10^{-3} mol L^{-1} BH_4^- on Au/C, Ag/C, Pt/C, and Pd/C, respectively. As can be noted, the BOR onset potential varies in the sequence Pt/C < Pd/C < Au/C < Ag/C, in full agreement with the results obtained using the DEMS flow cell. In particular, Au/C presents a much lower onset potential than Ag/C, illustrating its better BOR activity, but it is largely outperformed by both Pt/C and Pd/C. These figures also show the ring currents signals for the BH_3OH^- detection. As can be observed, Pt/C and Pd/C showed no ring signal in the low potential domain (−0.9; −0.5 V) both in positive and negative-going scans. Conversely, above ca. −0.45 V, the ring current increases significantly during potential excursions to 0.3 V, which still remains in the negative-going scan, and decreases to practically zero at ca. −0.45 V. Interestingly, the ring signal of the BH_3OH^- detection initiates at a potential very close to that of OH^- discharge (OH_{ads} formation) on the Pt/C and Pd/C surfaces. For Au/C and Ag/C, the detection of the BH_3OH^- can be observed as soon as the BOR starts. This behavior was observed in previous published works;[47,56] it defines a peak at ca. −0.1 V for Au/C and at ca. 0.0 V for Ag/C, and the detection decreases with the increase in the BOR oxidation current. Also for these cases, at potentials where Au or Ag-oxide(hydroxide) formation takes place, the BH_3OH^- oxidation current rises.

Considering the collection efficiency of the RRDE (ca. 23%), the expected ring current if all BH_4^- give one BH_3OH^- can be calculated according to eq 13:

$$I_{\text{ring, peak}} = I_{\text{disk, peak}} * \left(\frac{n_{\text{e/BH3OH−, max}}}{n_{\text{e/BH4−, max}}} \right) * \left(\frac{n_{\text{e/BH3OH−, at−0.72V}}}{n_{\text{e/BH3OH−, max}}} \right) * N \tag{13}$$

With:

$I_{\text{disk, peak}} \approx 6$ mA (see Figure 4); $n_{\text{e/BH3OH-, max}} = 6$ (electrons max per BH_3OH^-); $n_{\text{e/BH4-, max}} = 8$ (electrons max per BH_3OH^-); $n_{\text{e/BH3OH-, at}-0.72\text{ V}} = 3$ (electrons per BH_3OH^- for Au at −0.72 V); $N = 23\%$ (collection efficiency of the utilized RRDE electrode). Here, it is considered that (i) BH_4^- is present at 1.0 mmol L^{-1} in the RRDE experiments, which yields a diffusion limited plateau of ca. 6.0 mA for 8 electrons; (ii) any difference of diffusion coefficients between BH_4^- and BH_3OH^- is neglected (the latter is normally slightly smaller[58]).

Comparing the values of the expected ring current and the values measured experimentally, presented in Table 2, one can note that less than 2.5% of the BH_3OH^- species exit the disk electrode (compared to the amount of BH_4^- that reaches the disk). This is an indication that the effect of BH_3OH^- escape from the catalytic layer on the total faradic efficiency of the BOR is negligible. Considering that BH_3OH^- in solution are more easily oxidized than BH_4^- on all investigated electrocatalysts (except maybe for Pt[59,60]), it was expected that a very low amount of BH_3OH^- could exit the active layer, contrarily to what was expected for H_2 (as experimentally evidenced by DEMS).

Table 2. Measured and Expected Ring Currents (As Calculated from eq 13) for RRDE Experiments of the BOR on the Different Investigated Electrocatalysts[a]

electrocatalyst	peak ring current/mA	expected ring current if all BH_4^- give one BH_3OH^-/mA	% BH_3OH^- produced
Pt/C	0.012	0.51	2.3
Pd/C	0.013	0.51	2.5
Au/C	0.005	0.51	1.0
Ag/C	0.007	0.51	1.3

[a] RRDE collection efficiency = 23%.

From the two possible sources of loss in BOR faradaic efficiency (BH_3OH^- and H_2 escape), the results of Figures 3, 4, and Table 2 suggest that only the H_2 escape is quantitative (in first approximation). Therefore, the number of exchanged electrons per BH_4^- anion were calculated from the values of the total faradic current I_f and $|I_{\text{H2, eq}}|$ (eq 14) assuming the following hypotheses: (i) only the complete faradic BOR reaction (eq 1) or the heterogeneous hydrolysis reaction (eq 9) can take place (which assumes that all the BH_4^- is converted into BO_2^-, with no significant formation of partially hydrided B-containing species); either (ii) the H_2 produced via heterogeneous hydrolysis is completely lost to any electron generation (which means that all the generated electrons come from the BOR), or (iii) if some faradic current originates from the electrooxidation of H_2 produced via hydrolysis, it corresponds to the complete oxidation of each involved H_2 molecules and therefore does not produce any $m/z = 2$ mass signal.

$$n_{\text{e/BH4−}} = \frac{8I_f}{[I_f + |I_{\text{eq, H2}}|]} \tag{14}$$

Figure 5 presents the potential-dependent variation of the number of electrons exchanged per BH_4^- anion (calculated using eq 14). For Au/C, it monotonously increases from the BOR onset potential (−0.6 V) to reach 8 (which is the maximum value estimated by eq 14) between 0.0 and 0.2 V, and then it decreases to 6 at the positive vertex potential (0.4 V, in the Au-oxide region).[61,62] For Ag/C, the number of electrons starts to increase at ca. −0.1 V, which matches with the potential where the H_2 production decreases. In the particular

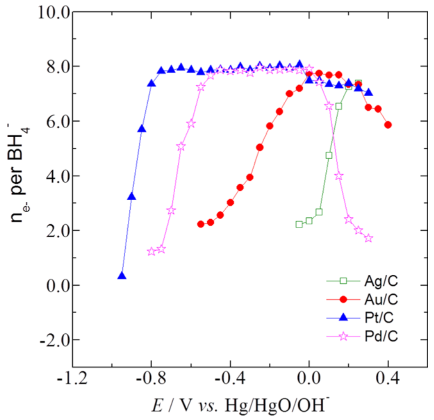

Figure 5. Calculated number of electrons for the BOR obtained using eq 14 (the considerations presented in the text).

case of this material, the onset potential for the BOR is at ca. −0.25 V. However, the H_2 detection was noisy between −0.25 and −0.15 V, leading to a high uncertainty in the estimation of the number of electrons. So, this interval was not considered in the calculations.

One can observe that, for Pt/C and Pd/C, the potential-dependent number of electrons exchanged per BH_4^- anion exhibits an abrupt increase above the BOR onset potential, reaching a plateau of eight electrons, nearly on the whole BOR potential range. This may be a consequence of the rapid hydrolysis suppression above the OCP or the rapid oxidation of any H* (eq 8) and H_2 (eq 10) species above the OCP. Knowing that the heterogeneous hydrolysis is a chemical reaction, which shall not directly depend on the electrode potential, and that Pt and Pd are highly active for both H* and H_2 oxidation, the abrupt decrease in the H_2 detection above ca. −0.9 is more likely due to the rapid consumption of H* or H_2 species by electrochemical oxidation. Here, one can, however, not rule out that the OCP on Pt and Pd consists of a mixed potential (BH_4^- oxidation and H_2 evolution occurring simultaneously at OCP) and, in such scenario, the production (and detection) of H_2 would also likely vary with the potential around OCP. Indeed, this seems to be the most likely explanation for the open circuit potential. The fact that H_2 production was also detected in the Pt-oxide region using sputtered Pt electrodes in stagnant electrolyte DEMS cell (at higher BH_4^- concentration, 10 mmol L^{-1})[44] also militates in favor of this scenario—Pt-oxides being incapable to ionize H_2. However, one may not rule out that the hydrolysis pathway depends on the borohydride concentration, which has already been stated in refs 63,64, and it will not be discussed further here.

According to principles investigated for other catalytic and electrocatalytic reactions, the reactivity of metals can be related to their *d*-band center.[65−67] Metals that offer stronger adsorption of BH_4^- ions may result in a faster B−H bond breaking, resulting in fast H* formation, producing H_2 around or below OCP (eq 7) and faradaic current through eq 8 above OCP. Conversely, metals that offer weaker adsorption may result in lower activity for the B−H bond breaking, corresponding to lower H_2 formation,[68,69] and conducts to a larger H_2 production above OCP, due to the combination of eqs 4, 5, and 7. Usually, these surfaces are incapable to efficiently valorize H* or H_2 species via electrochemical oxidation.

Considering the DEMS and the RRDE results, and previous published data for the BOR,[70−73] the following discussion can be addressed: It is known that Au/C and Ag/C have lower values of *d*-band center (−4.30 eV and −3.65 eV, respectively), when compared to those for Pt/C and Pd/C (−2.25 eV and −1.85 eV, respectively). DFT calculations[34] have indicated that the BH_4^- bonds are activated by the catalysts, and this activation is relatively slow on the Au(111) surface and fast on the Pt(111) surface, even at potential values as low as −0.89 V. Therefore, the activity for the B−H dissociation is a key factor for determining the relative activity of an electrocatalyst and explains why the reaction onset is lower for Pt(111) in comparison to Au(111). Therefore, a similar trend should proceed when comparing Ag(111) and Pd(111). This trend was, in fact, experimentally observed in the work, the BOR activity increasing in the sequence: Au/C < Ag/C ≪ Pd/C < Pt/C.

For Au/C and Ag/C, at low potentials, the BOR is very slow because their reactivity (low *d-band* center) does not prevail in comparison to the electrostatic repulsion between these negative species and the negatively charged surface. Thus, the dissociative BH_4^- adsorption, with the B−H bond dissociation, takes place only with a slow rate, and therefore, the BOR is not accelerated. At low potentials, a very low faradaic current is observed, and no free (or nondetectable) H_2 or BH_3OH^- is shown by DEMS and RRDE, respectively. As observed in Figure 3a,b and Figure 4a,b, upon increasing the electrode potential, the BOR initiates. This can be associated with an increase in the adsorption strength of the BH_4^- species on the Au/C and Ag/C surfaces due to a diminished electrostatic repulsion, thereby enabling the B−H bonds dissociation. Concomitantly, the DEMS results show an apparent acceleration of the heterogeneous hydrolysis, producing a massive amount of H_2, and the RRDE measurements show BH_3OH^- formation. Knowing that neither Au nor Ag surfaces are prone to ionize hydrogen, the released H_2 cannot be valorized by these metals via electrooxidation. Considering the high overpotential where the H_2 is detected for Au/C and Ag/C, it seems unlikely that the detected H_2 comes from H*, but probably more likely from direct heterogeneous hydrolysis (without H* intermediate formation). The superposition of the BH_3OH^- escape signals (RRDE) and H_2 escape signals (DEMS) point out a possible link between BH_3OH^- and H_2. At low overpotentials (oxide-free region), in the BOR onset potential region, the faradaic current may arise from partial oxidation of BH_4^-, according to eqs 15−17:

$$BH_4^- + 2* \rightarrow BH_3* + H* + e^- \quad (15)$$

$$BH_3* + OH^- \rightarrow BH_3OH* + e^- \quad (16)$$

$$BH_3OH* + OH^- \rightarrow BH_3OH^- + OH* \quad (17)$$

and in parallel with reactions involving hydrolysis, such as those represented in eqs 18 and 19:

$$BH_4^- + H_2O \rightarrow BH_3OH^- + H_2 \quad (18)$$

$$BH_3OH^- + H_2O \rightarrow BO_2^- + 3H_2 \quad (19)$$

Pt/C and Pd/C have higher *d*-band center, and so, they feature higher reactivity. As a consequence, the electrostatic repulsion at low potentials is overcome, and the BH_4^- species can adsorb on the Pt/C and Pd/C surfaces and undergo B−H bond breaking. Therefore, complete or partial dissociative adsorption of BH_4^- takes place at low potentials (eqs 4 or 15). As observed by online DEMS experiments, at the OCP, there is a significant production of H_2, and when the electrode potential is higher than −0.9 V, the reaction initiates and the H_2 detection signal is abruptly decreased. This suggests that, in the case of Pt/C and Pd/C, H_2 production occurs from recombination of H* more than from direct heterogeneous hydrolysis (no BH_3OH^- are detected at low potential on Pt/C and Pd/C, Figure 4). Contrarily to what was observed for Au/C and Ag/C, if BH_3* species are formed, they may remain adsorbed on the metal surfaces at this low potential domain, and evolve toward the more stable BH* species, as no signal of BH_3OH^- detection was shown during the RRDE measurements (as forecasted by Rostamikia and Janik[34]). As faradaic current is observed at low potential domains for Pt/C and Pd/C, the BOR may proceed via dissociative adsorption of BH_4^- producing H* and BH_3*, following eq 15 or, more probably, BH* species, according to eq 4. However, the H* or H_2

(formed from the recombination of two neighboring H*, at low potentials) are right away oxidized (eq 8 or 10), resulting in faradaic current at low potentials.

This may occur in parallel with hydrolysis steps but now involving adsorbed species, according to eqs 20 and 21:

$$BH_3* + H_2O \rightarrow BOH* + 2H_2 \qquad (20)$$

$$BH_3* + H_2O \rightarrow BH_2OH* + H_2 \qquad (21)$$

(with no bulk BH_3OH^- being detected by RRDE, but with H_2 being detected by DEMS)

For all the investigated electrocatalysts, upon increasing the electrode potential, the detected BH_3OH^- and H_2 may come from a parallel reaction of hydrolysis of the BH_4^- or other partial oxidized species on oxide-containing metal surface,[74] following reactions similar to those presented in eqs 18 and 19. However, additional investigations are needed in order to elucidate the heterogeneous hydrolysis reaction on metal oxide surfaces. Here, it is worthwhile to mention that all these metal oxides are inactive for the H_2 eletrooxidation, and therefore, they can not valorize the produced H_2 molecules at higher potentials. Nevertheless, such condition of high potential is irrelevant for the anode of DBFC.

■ CONCLUSION

The results presented herein showed that the BOR onset potential followed the order: Pt/C < Pd/C < Au/C < Ag/C. For Au/C and Ag/C, the H_2 production, due to hydrolysis, presented a peak of production in the potential region of the first branch of the BOR wave, and it showed an additional increase in the metal oxide region, mainly noticed for Au/C. This behavior was also followed by the BH_3OH^- species production. The faradaic efficiencies for Au/C and Ag/C monotonously rise with the potential and then reached eight electrons per BH_4^- (H_2 detection being minimum). Pt/C and Pd/C showed accentuated H_2 detection at the OCP, with a sharp decrease to practically zero after the BOR onset and with an increase only in the Pt and Pd-oxide region. The number of exchanged electrons per BH_4^- reached eight just above the BOR onset potential. Interestingly and contrarily to what was observed for Au/C and Ag/C, the RRDE measurements showed BH_3OH^- production only at higher potentials (oxide region). These results were explained on the basis of the higher reactivity of Pt/C and Pd/C for the BOR, in which BH_3-like species remain adsorbed and hydrogen is consumed via electrooxidation on their surfaces, at low potentials. On the other hand, Au/C and Ag/C, possessing lower reactivity (lower *d*-band center), the BH_3-like species, produced in the first reaction steps, desorb from their surfaces and are detected at the ring. Concomitantly, H_2 is formed via recombination of adsorbed hydrogen atoms (at low potentials), and it can be detected by the mass spectrometer, as these materials are relatively inactive for the hydrogen oxidation reaction.

■ AUTHOR INFORMATION

Corresponding Author

*E-mail: fabiohbl@iqsc.usp.br. Tel.: +55 16 3373 8681. Fax. +55 16 3373 9952.

Notes

The authors declare no competing financial interest.

■ ACKNOWLEDGMENTS

The authors gratefully acknowledge financial support from CAPES-COFECUB (Project No. 598/08), FAPESP (Fundação de Amparo à Pesquisa do Estado de São Paulo) – Sao Paulo Research Foundation – FHBL (Grant Nos. 2011/50727-9 and 2013/16930-7) and AMP (Grant Nos. 2011/03672-4 and 2012/00877-7), and CNPq (Conselho Nacional de Desenvolvimento Científico e Tecnológico) – FHBL – (Grant No. 306213/2013-3). M.C. thanks the French IUF for its support. P.Y.O. is grateful to IDS FunMat for his Ph.D. grant (Project 2012 LF).

■ REFERENCES

(1) Zhu, M.; Park, J.; Sastry, A. M. *J. Electrochem. Soc.* **2011**, *158*, A1155–A1159.

(2) Kordesch, K., Simader, G. In *Fuel Cells And Their Applications*; Wiley-VCH: New York, 1996; p 375.

(3) Fakioglu, E.; Yurum, Y.; Veziroglu, Tn. *Int. J. Hydrogen Energy* **2004**, *29*, 1371–1376.

(4) Ma, J.; Choudhury, N. A.; Sahai, Y. *Renewable Sustainable Energy Rev.* **2010**, *14*, 183–199.

(5) Molina-Concha, M. B.; Chatenet, M.; Maillard, F.; Ticianelli, E. A.; Lima, F. H. B.; De Lima, R. B. *Phys. Chem. Chem. Phys.* **2010**, *12*, 11507–1151.

(6) Molina-Concha, M. B.; Chatenet, M.; Ticianelli, E. A.; Lima, F. H. B. *J. Phys. Chem. C* **2011**, *115*, 12439–12447.

(7) Adzic, R. R., Lima, F. H. B. In *Handbook of Fuel Cells*; Vielstich, W., Hukokawa, H., Gasteiger, H. A., Eds.; John Wiley & Sons: New York, 2009; Vol. *5*, pp 5–17.

(8) Santos, D. M. F.; Sequeira, C. A. C. *J. Electrochem. Soc.* **2012**, *159*, B126–B132.

(9) Cheng, H.; Scott, K. *J. Power Sources* **2006**, *160*, 407–412.

(10) Feng, R. X.; Dong, H.; Wang, Y. D.; Ai, X. P.; Cao, Y. L.; Yang, H. X. *Electrochem. Commun.* **2005**, *7*, 449–452.

(11) Raman, R. K.; Choudhury, N. A.; Shukla, A. K. *Electrochem. Solid-State Lett.* **2004**, *7*, A488–A491.

(12) Raman, R. K.; Prashant, S. K.; Shukla, A. K. *J. Power Sources* **2006**, *162*, 1073–1076.

(13) Liu, B. H.; Li, Z. P.; Arai, K.; Suda, S. *Electrochim. Acta* **2005**, *50*, 3719–3725.

(14) Celik, C.; San, F. G. B.; Sarac, H. I. *J. Power Sources* **2008**, *185*, 197–201.

(15) Cheng, H.; Scott, K.; Lovell, K. *Fuel Cells* **2006**, *6*, 367–375.

(16) Li, Z. P.; Liu, B. H.; Arai, K.; Suda, S. *J. Alloys Compd.* **2005**, *648*, 404–406.

(17) Ma, J.; Choudhury, N. A.; Sahai, Y. *Renewable Sustainable Energy Rev.* **2010**, *14*, 183–199.

(18) Demirci, U. B. *J. Power Sources* **2007**, *169*, 239–246.

(19) Yu, X.; Manthiram, A. *Appl. Catal., B* **2015**, *165*, 63–67.

(20) McLafferty, J.; Colominas, S.; Macdonald, D. D. *Electrochim. Acta* **2010**, *56*, 108–114.

(21) Gyenge, E. L.; Oloman, C. W. *J. Appl. Electrochem.* **1998**, *28*, 1147–1151.

(22) Santos, D. M. F.; Sequeira, C. A. C. *Int. J. Hydrogen Energy* **2010**, *35*, 9851–9861.

(23) Shu, C.; Sun, T.; Jia, J.; Lou, Z. *Fuel* **2013**, *113*, 187–195.

(24) Santos, D. M. F.; Sequeira, C. A. C. *Renewable Sustainable Energy Rev.* **2011**, *15*, 3980–4001.

(25) Chatenet, M., Molina-Concha, M. B., Parrour, G., Diard, J. -P., Lima, F. H. B., Ticianelli, E. A. In *Boron Hydrides, High Potential Hydrogen Storage Materials*; Demirci, U., Miele, P., Eds.; Nova Science Publisher: New York, 2010; pp 103–136.

(26) Gardiner, J. A.; Collat, J. W. *J. Am. Chem. Soc.* **1965**, *87*, 1692–1694.

(27) Elder, J. P.; Hickling, A. H. *Trans. Faraday Soc.* **1962**, *58*, 1852–1864.

(28) Morris, J. H.; Gysling, H. J.; Reed, D. *Chem. Rev.* **1985**, *85*, 51–76.
(29) Santos, D. M. F.; Sequeira, C. A. C. *Electrochim. Acta* **2010**, *55*, 6775–6781.
(30) Geng, X.; Zhang, H.; Ye, W.; Ma, Y.; Zhong, H. *J. Power Sources* **2008**, *185*, 627–632.
(31) Coowar, F. A.; Vitins, G.; Mepsted, G. O.; Waring, S. C.; Horsfall, J. A. *J. Power Sources* **2008**, *175*, 317–324.
(32) Rostamikia, G.; Mendoza, A. J.; Hickner, M. A.; Janik, M. J. *J. Power Sources* **2011**, *196*, 9228–9237.
(33) Rostamikia, G.; Janik, M. J. *J. Electrochem. Soc.* **2009**, *156*, B86–B92.
(34) Rostamikia, G.; Janik, M. J. *Energy Environ. Sci.* **2010**, *3*, 1262–1274.
(35) Rostamikia, G.; Janik, M. J. *Electrochim. Acta* **2010**, *55*, 1175–1183.
(36) Hristov, G.; Mitov, M.; Rashkov, R.; Hristov, S.; Popov, A. *Bulg. Chem. Commun.* **2008**, *40*, 306–309.
(37) Wang, L.; Ma, C.; Sun, Y.; Suda, S. *J. Alloys Compd.* **2005**, *391*, 318–322.
(38) Paschoalino, W. J.; Ticianelli, E. A. *Int. J. Hydrogen Energy* **2013**, *38*, 7344–7352.
(39) Paschoalino, W. J.; Thompson, S. J.; Russell, A. E.; Ticianelli, E. A. *ChemPhysChem* **2014**, *15*, 2170–2176.
(40) Grinberg, V. A.; Mayorova, N. A.; Korlyukov, A. A.; Pasynskii, A. A. *Russ. J. Electrochem.* **2010**, *46*, 1289–1296.
(41) Parrour, G.; Chatenet, M.; Diard, J.-P. *Electrochim. Acta* **2010**, *55*, 9113–9124.
(42) Molina-Concha, M. B.; Chatenet, M. *Electrochim. Acta* **2009**, *54*, 6119–6129.
(43) Molina-Concha, M. B.; Chatenet, M. *Electrochim. Acta* **2009**, *54*, 6130–6139.
(44) Lima, F. H. B.; Pasqualeti, A. M.; Molina-Concha, M. B.; Chatenet, M.; Ticianelli, E. A. *Electrochim. Acta* **2012**, *84*, 202–212.
(45) Chatenet, M.; Lima, F. H. B.; Ticianelli, E. A. *J. Electrochem. Soc.* **2010**, *157*, B697–B704.
(46) Baltruschat, H. *J. Am. Soc. Mass Spectrom.* **2004**, *15*, 1693–1706.
(47) Krishnan, P.; Yang, T.-H.; Advani, S. G.; Prasad, A. K. *J. Power Sources* **2008**, *182*, 106–111.
(48) Turkevich, J.; Hillier, J.; Stevenson, P. C. *Discuss. Faraday Soc.* **1951**, *11*, 55–75.
(49) Brown, K. R.; Walter, D. G.; Natan, M. J. *Chem. Mater.* **2000**, *12*, 306–313.
(50) Kristian, N.; Wang, X. *Electrochem. Commun.* **2008**, *10*, 12–15.
(51) West, A. R. In *Solid State Chemistry and its applications*; Wiley: New York, 1984; pp 240–247.
(52) Guilminot, E.; Corcella, A.; Charlot, F.; Maillard, F.; Chatenet, M. *J. Electrochem. Soc.* **2007**, *154*, B96–B105.
(53) De Souza, J. P. I.; Queiroz, S. L.; Nart, F. C. *Quim. Nova* **2000**, *23*, 384–391.
(54) Bittins-Cattaneo, B., Cattaneo, E., Konigshoven, P., Vielstich, W. In *Electroanalytical Chemistry - A Series of Advances*; Bard, A. J., Ed.; Marcel Dekker: New York, 1991; p 181.
(55) Ianniello, R.; Schmidt, V. M.; Bunsen-Ges, Ber. *Phys. Chem.* **1995**, *99*, 83–86.
(56) Chatenet, M.; Molina-Concha, M. B.; El-Kissi, N.; Parrour, G.; Diard, J.-P. *Electrochim. Acta* **2009**, *54*, 4426–4435.
(57) Parrour, G.; Chatenet, M.; Diard, J.-P. *Electrochim. Acta* **2010**, *55*, 9113–9124.
(58) Molina-Concha, M. B.; Chatenet, M.; Lima, F. H. B.; Ticianelli, E. A. *Electrochim. Acta* **2013**, *89*, 607–615.
(59) Nagle, L. C.; Rohan, J. F. *Electrochem. Solid-State Lett.* **2005**, *8*, C77–C80.
(60) Nagle, L. C.; Rohan, J. F. *J. Electrochem. Soc.* **2006**, *153*, C773–C776.
(61) Gyenge, E. *Electrochim. Acta* **2004**, *49*, 965–978.
(62) Mirkin, M. V.; Yang, H.; Bard, A. J. *J. Electrochem. Soc.* **1992**, *139*, 2212–2217.
(63) Freitas, K. S.; Molina-Concha, M. B.; Ticianelli, E. A.; Chatenet, M. *Catal. Today* **2011**, *170*, 110–119.
(64) Olu, P.-Y.; Barros, C. R.; Job, N.; Chatenet, M. *Electrocatalysis* **2014**, *5*, 288–300.
(65) Hammer, B.; Nørskov, J. K. *Adv. Catal.* **2000**, *45*, 71–129.
(66) Greeley, J.; Nørskov, J. K.; Mavrikakis, M. *Annu. Rev. Phys. Chem.* **2002**, *53*, 319–348.
(67) Kitchin, J. R.; Nørskov, J. K.; Barteau, M. A.; Chen, G. *J. Chem. Phys.* **2004**, *120*, 10240–10246.
(68) Zhang, J.; Vukmirovic, M. B.; Xu, Y.; Mavrikakis, M.; Adzic, R. R. *Angew. Chem., Int. Ed.* **2005**, *44*, 2132–2135.
(69) Lima, F. H. B.; Zhang, J.; Shao, M. H.; Sasaki, K.; Vukmirovic, M. B.; Ticianelli, E. A.; Adzic, R. R. *J. Phys. Chem. C* **2007**, *111*, 404–410.
(70) Olu, P.-Y.; Bonnefont, A.; Rouhet, M.; Bozdech, S.; Job, N.; Chatenet, M.; Savinova, E. R.; *Electrochim. Acta*, *in press*, 10.1016/j.electacta.2015.02.158.
(71) Olu, P.-Y.; Barros, C.; Job, N.; Chatenet, M. *Electrocatalysis* **2014**, *5*, 288–300.
(72) Escano, M. C. S.; Arevalo, R. L.; Gyenge, E.; Kasai, H. J. *J. Phys.: Condens. Matter* **2014**, *26*, 353001–353015.
(73) Chatenet, M.; Micoud, F.; Roche, I.; Chainet, E. *Electrochim. Acta* **2006**, *51*, 5459–5467.
(74) Machado, E. G.; Sitta, E.; Lima, F. H. B.; Lee, J.; Varela, H. *Electrochem. Commun.* **2012**, *16*, 107–109.